Luminescent Behavior of the K_2SiF_6:Mn^{4+} Red Phosphor at High Fluxes and at the Microscopic Level

Heleen F. Sijbom,[a,b,z] Jonas J. Joos,[a,b] Lisa I. D. J. Martin,[a,b] Koen Van den Eeckhout,[a,b] Dirk Poelman,[a,b,*] and Philippe F. Smet[a,b,*,z]

[a]*LumiLab, Department of Solid State Sciences, Ghent University, Ghent, Belgium*
[b]*Center for Nano- and Biophotonics (NB-Photonics), Ghent University, Ghent, Belgium*

Phosphor-converted white light-emitting diodes (LEDs) are becoming increasingly popular for general lighting. The non-rare-earth phosphor K_2SiF_6:Mn^{4+}, showing promising saturated red d-d-line emission, was investigated. To evaluate the application potential of this phosphor, the luminescence behavior was studied at high excitation intensities and on the microscopic level. The emission shows a sublinear behavior at excitation powers exceeding 40 W/cm^2, caused by ground-state depletion due to the ms range luminescence lifetime. The thermal properties of the luminescence in K_2SiF_6:Mn^{4+} were investigated up to 450 K, with thermal quenching only setting in above 400 K. The luminescence lifetime decreases with increasing temperature, even before thermal quenching sets in, which is favorable to counteract the sublinear response at high excitation intensity. A second, faster, decay component emerges above 295 K, which, according to crystal field calculations, is related to a fraction of the Mn^{4+} ions incorporated on tetragonally deformed lattice sites. A combined investigation of structural and luminescence properties in a scanning electron microscope using energy-dispersive X-ray spectroscopy and cathodoluminescence mappings showed both phosphor degradation at high fluxes and a preferential location of the light outcoupling at irregularities in the crystal facets. The use of K_2SiF_6:Mn^{4+} in a remote phosphor configuration is discussed.

Most phosphor-converted white LEDs contain phosphors doped with rare earths such as divalent europium and trivalent cerium. These ions feature relatively broad emission bands based on the parity allowed 5d-4f transition. They are often easily excited with blue light and can show high quantum efficiency, even at elevated temperature. To improve the color rendering of white LEDs, red phosphors are added to the traditional blue LED and yellow $Y_3Al_5O_{12}$:Ce (YAG:Ce) phosphor combination. These red phosphors need to be stable and have a high quantum efficiency. The emission spectrum should both be sufficiently red (>600 nm) and well within the eye sensitivity curve, to obtain a high luminous efficacy.[1] Sulfide phosphors doped with Eu^{2+}, such as (Ca,Sr)S:Eu^{2+} are known for their efficient red emission,[2] but they lack stability in humid environments and the eye sensitivity is low for part of their broad emission band.[3] Nitride phosphors doped with Eu^{2+} are often chemically more stable, but their synthesis at high pressure and temperature is a drawback.[4] Most europium-doped nitride phosphors show a relatively broad emission band.[5,6]

Cost and supply issues of the rare-earth materials pave the way for transition-metal-doped phosphors.[7] In particular the Mn^{4+} ion is a promising alternative for Eu^{2+} as it shows line emission from parity and spin-forbidden d-d transitions in the red and near-infrared spectral region. Investigation of the optical properties of the Mn^{4+} dopant showed that fluoride hosts are preferred for LED phosphors over oxide hosts, since only the ionic nature of fluorides results in a sufficiently small nephelauxetic effect, maintaining the energy of the emitting $^2E_g \rightarrow {}^4A_{2g}$ transition within the visible part of the spectrum, corresponding to red emission with a zero phonon line in the 617–624 nm range.[8,9] For instance in the oxide phosphors, $GdAlO_3$:Mn^{4+}, $SrTiO_3$:Mn^{4+} and $Y_2Sn_2O_7$:Mn^{4+} the emission is well beyond 650 nm and thus unsuitable for visible displays or lighting.[10–12]

The interest in K_2SiF_6:Mn^{4+} as a red phosphor started with the development of a synthesis method by Adachi and Takahashi, etching Si wafers in HF in the presence of $KMnO_4$.[13,14] This ambient wet chemical synthesis is cost effective compared to standard phosphor syntheses, which take place at high firing temperatures in controlled atmosphere. The synthesis of K_2SiF_6:Mn^{4+} was further developed with etching of crushed quartz schist[15] and silica glasses.[16] Variations in the synthesis method led to the synthesis of the host lattice K_2SiF_6 from etching SiO_2 powder with HF in the presence of KF.[17] In the presence of $KMnO_4$, the Mn^{4+}-doped phosphor precipitates from the etching solution.

This phosphor has already been subject of detailed investigations. The electronic structure and mechanical properties of the host compound were obtained from density functional theory (DFT) calculations.[18] From DFT, an electronic bandgap around 8 eV was found. Takahashi and Adachi reported an optical bandgap of 5.6 eV, obtained from diffuse-reflectance spectroscopy.[9] This is surprisingly low compared to the DFT value. It is possible that the observed absorption band, which occurs at the edge of the spectral range of the used detector, is due to intrinsic defects, rather than fundamental absorption.[9,18]

The multiplet structure originating from the $3d^3$ configuration has been investigated in the framework of crystal field theory[16] and by coupling single-particle orbitals, obtained from Hartree–Fock–Slater calculations.[19] Both investigations started from the octahedral symmetry of the Si^{4+} site of the K_2SiF_6 host. The vibronic fine structure of the Mn^{4+} emission and excitation spectra has been described in detail.[9,20]

Applications for K_2SiF_6:Mn^{4+} and other Mn^{4+}-doped fluoride phosphors are found in warm-white LEDs,[21,22] following the inclusion of K_2SiF_6:Mn^{4+} in several patents.[23–26] No prior research was reported on the influence of a high excitation intensity on the K_2SiF_6:Mn^{4+} phosphor. The long, ms range, lifetime of the d-d transitions in Mn^{4+} can cause problems when Mn^{4+}-doped materials are used in high-power LEDs,[27] similar to the case of Mn^{2+}.[28] Until now luminescence-lifetime measurements were only performed for low and high dopant concentrations[27] in the temperature range of 20–300 K.[29,30] We performed both luminescence-lifetime and thermal-quenching measurements up to 450 K, which is important in view of its application in high-power LEDs. Crystal field calculations were performed for theoretical support of experimental findings. We combined cathodoluminescence with SEM-EDX mappings to evaluate the chemical composition, degradation and light output of phosphor particles at the microscopic level.

*Electrochemical Society Active Member.
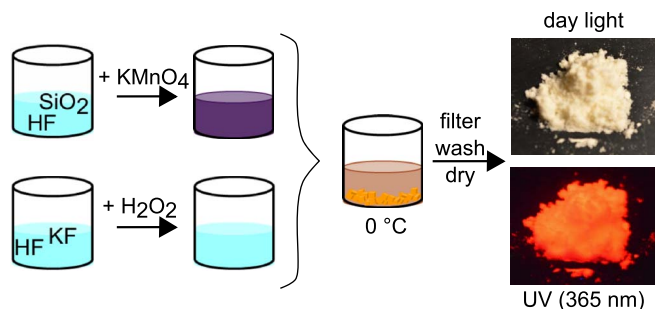[z]E-mail: Heleen.Sijbom@UGent.be; Philippe.Smet@UGent.be

Figure 1. Two step synthesis of K_2SiF_6:Mn^{4+} in HF at 0°C. Appearance of K_2SiF_6:Mn^{4+} under day light and UV illumination (right).

Figure 2. XRD measurement of the red phosphor K_2SiF_6:Mn^{4+} (b), compared with the reference pattern (ICSD 29407) for K_2SiF_6 (a).

Experimental

The phosphor particles were synthesized by solution synthesis in 40% HF (Sigma Aldrich), according to the procedure described by Nguyen.[31] SiO_2 (99.5%, Alfa Aesar) was dissolved in HF at room temperature. $KMnO_4$ (98%, Alfa Aesar) was added to this solution, such that a dopant concentration of 8% of Mn is obtained. In a separate solution, KF (99%, Alfa Aesar) was dissolved in HF and 35% H_2O_2 (Sigma Aldrich) was added. The two solutions were mixed in an ice bath, where the phosphor particles precipitated. The precipitate was washed with 20% HF and ethanol and dried at room temperature in air, resulting in a light-yellow powder (Figure 1).

Powder X-ray diffraction (XRD) patterns were measured on a Siemens D5000 diffractometer (40 kV, 40 mA) using Cu $K\alpha_1$ radiation. Photoluminescence (PL) excitation and emission spectra were measured using an Edinburgh FS920 fluorescence spectrometer with a monochromated 450 W Xe arc lamp as excitation source. Low temperature PL measurements were performed using an Oxford Optistat CF cryostat. An integrating sphere (LabSphere GPS-SL series) was used to measure the internal and external quantum efficiency of the phosphor upon LED excitation at 450 nm. For these measurements, Al_2O_3 was used as a white reflective standard. SEM-EDX-CL measurements were performed with a Hitachi S-3400 N scanning electron microscope (SEM), equipped with a Thermo Scientific Noran 7 energy-dispersive X-ray detector (EDX). Furthermore, cathodoluminescence (CL) was collected with an optical fiber and analyzed using an EMCCD camera (Princeton Instruments ProEM 16002), attached to a spectrograph (Princeton Instruments Acton SP2358). Thermal-quenching and saturation measurements were performed in a home built set-up using the same EMCCD camera and spectrograph. A blue 445 nm 600 mW laser diode was used as excitation source for the saturation measurements. Sample temperatures were measured using a FLIR A35sc thermal infrared (IR) camera. Decay profiles were collected as a function of temperature using an Oxford Optistat CF cryostat. A pulsed nitrogen laser with emission at 337 nm was used as excitation source in combination with an intensified CCD detector (Andor Instruments DH720) coupled to a 0.5 m monochromator. Simulations of phosphor combinations for white LEDs were performed using the NIST-CQS software.[32–34]

Computational Method

The electronic structure of Mn^{4+} in K_2SiF_6 was described within the formalism of crystal field theory (CFT). An effective Hamiltonian, accounting for all the relevant interactions concerning the $3d^3$ configuration was diagonalized. All terms in the Hamiltonian consist of an exactly calculable factor containing an angular integral and a radial integral for which no straightforward analytical expression is available. Empirical parameters are typically used for the latter. In this case, the effective Hamiltonian is written as:[35,36]

$$\mathcal{H} = E_0 + \sum_{k=2,4} f_k F^k + \sum_{k=2,4} \sum_{q=-k}^{k} B_{kq} C_{kq} + \zeta_{nd} A_{so} + \alpha L (L + 1)$$
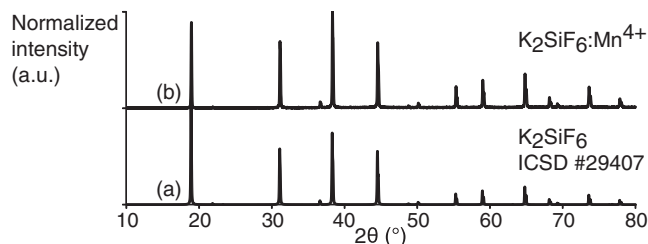
[1]

Herein, the first term contains the spherical symmetric contributions of all interactions. In practice, the obtained energy spectrum is shifted to put the lowest eigenvalue at zero. The second term represents the inter-electronic coulomb repulsion and is traditionally written in terms of Slater–Condon parameters which transform according to the irreducible representations (irrep) of the three-dimensional rotation group. In the case of partially filled d and f shells, it is however more convenient to introduce Racah parameters which transform properly for the complete Lie group chain that describes the electron configuration.[37] Two Racah parameters, B and C are required for nd^N configurations. The third term is the crystal field potential. Point symmetry of the defect dictates which crystal field parameters, B_{kq} are nonzero.[36] Alternative parameterizations can be found in literature (see further). The fourth term, which is often neglected in the case of 3d transition-metal ions, represents spin–orbit interaction. The last term, first introduced by Trees and Racah, corrects for the effect of two-body configuration interactions. Herein, L signifies the total orbital angular momentum of the electronic state. It has been shown that the inclusion of this additional term in Eq. 1 improves the correspondence between calculated and experimental spectra.[38–40]

The crystal field calculations were performed using an in-house developed Python program.[41] A Russel–Saunders basis, $^{2S+1}L_{J(M_J)}$, was used for this purpose. In the case of a d^3 configuration, the basis is 120 dimensional.

Results and Discussion

Structure.— All the reflections in the measured X-ray diffraction (XRD) pattern in Figure 2 can be assigned to the standard pattern of K_2SiF_6 (cubic space group $Fm\bar{3}m$). Although Mn^{4+} doping induces a larger ion (53 pm) in the lattice site of Si^{4+} (40 pm),[42] no significant shift of the reflections caused by the doping is observed.

The cubic crystal structure is also clear from the scanning electron microscope (SEM) picture in Figure 3, where cubic and octahedral particles with a diameter of 2–10 μm can be seen. Truncation of cubic particles leads to truncated cubes, cuboctahedrons and octahedral crystals. This truncation can be beneficial for the luminescence output of the particles, as will be explained later. Energy-dispersive X-ray (EDX) analysis shows a homogeneous elemental distribution of K, Si, F and Mn. No clusters of Mn are observed, so the doping is homogeneous over the particles within the detection limit and spatial resolution of EDX. The dopant concentration is 1.5 ± 0.3% of the amount of Si, as found from EDX analysis. Since the Mn concentration is 8% of the Si concentration in the precursor solutions, it seems that only a limited fraction of Mn is incorporated in the phosphor crystals during the synthesis.

Luminescence.— The room-temperature photoluminescence spectra (Figure 4a) show narrow emission bands due to the $^2E_g \rightarrow {}^4A_{2g}$ spin-forbidden transitions in Mn^{4+}.[8] Its line emission at 630 nm is perceived as saturated red and the eye sensitivity is still quite high in this wavelength range, which is beneficial for lighting applications. Two broad excitation bands are present corresponding to the $^4A_{2g} \rightarrow {}^4T_{2g}$ and $^4A_{2g} \rightarrow {}^4T_{1g}$ spin-allowed transitions.[8] The main excitation band is centered around 455 nm, which is ideal for blue-LED excitation at
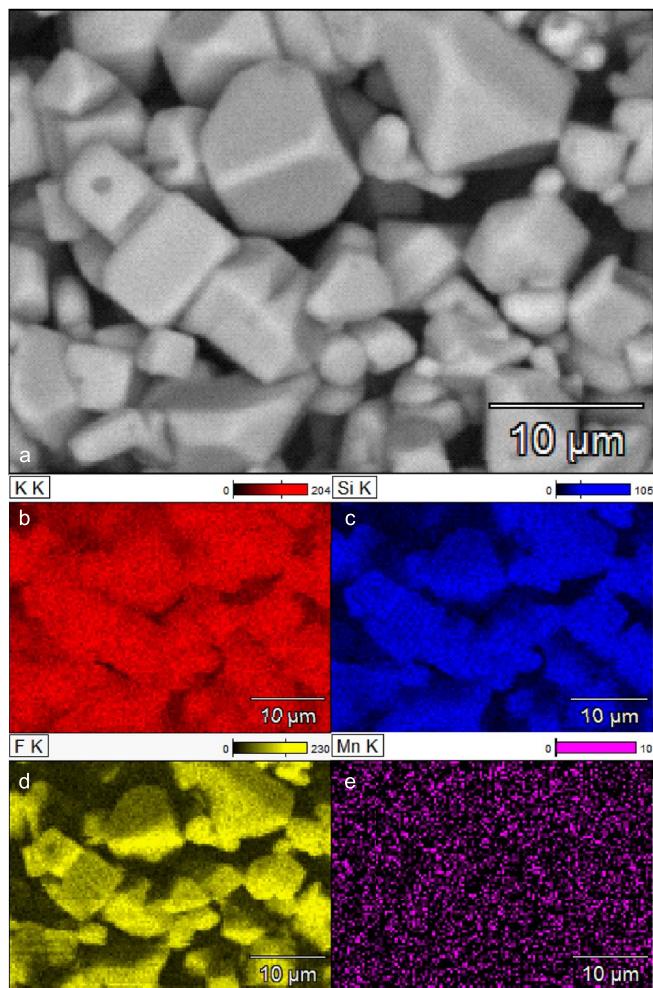
Figure 3. Low-vacuum scanning electron microscopy image from backscattered electron detection (a) and energy-dispersive X-ray mappings of K_2SiF_6:Mn^{4+} (b–e).
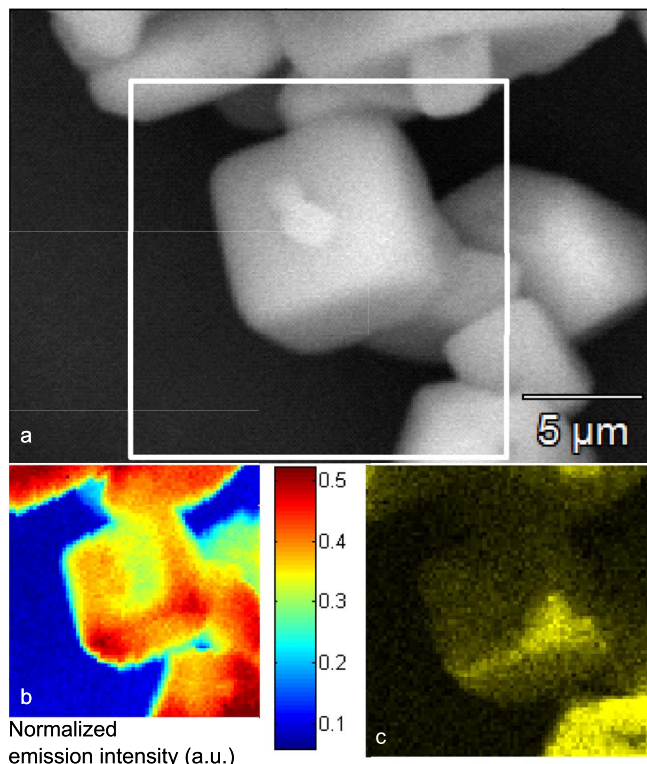
Figure 5. SEM picture (a), cathodoluminescence mapping (b), and F Kα EDX mapping of K_2SiF_6:Mn^{4+} particles (c).

450–460 nm. No excitation bands are present at wavelengths above 500 nm, which prevents reabsorption of yellow and green phosphor emission in a phosphor-converted white LED.

Additionally, the PL spectra were measured at 10 K (Figure 4b). The vibronic fine structure is clearly visible in the case of the $^2E_g \rightarrow ^4A_{2g}$ and $^4A_{2g} \rightarrow ^4T_{2g}$ transitions. For the $^2E_g \rightarrow ^4A_{2g}$ transition, the zero phonon line (ZPL) is located at 620.5 nm. The location of the ZPL is hard to determine in case of the $^4A_{2g} \rightarrow ^4T_{2g}$ transition because in addition to the occurrence of the different phonon-assisted transitions, the $^4T_{2g}$ electronic energy level is expected to be split due to low-symmetry crystal field components and the spin–orbit interaction (see further).

The internal quantum efficiency (IQE), defined as the ratio between the number of emitted and absorbed photons, is 42%. About 25% of the incident photons at 450 nm are absorbed by the phosphor, which limits the external quantum efficiency. Further improvement of the IQE is realistic, since values of 74%[43] and 80%[21] have been reported earlier.

The SEM picture in Figure 5a shows the representative particles selected for CL and EDX mappings. The CL mapping in Figure 5b shows a preferential location of the light output on certain edges of the cubic particle. Rotating the particle with respect to the light-collecting optical fiber leads to essentially the same spatial emission pattern. The light outcoupling is maximal at the lower crystal edge, while excitation with the electron beam in the center of the top surface leads to lower CL emission intensity, independent of the location of the optical fiber. At the lower-right corner, the cube is truncated forming an octahedral crystal face, as is more clearly seen in the fluorine Kα EDX mapping in Figure 5c. As the low-energy F Kα X-rays have a short attenuation length in the K_2SiF_6 lattice, geometrical aspects influence the relative number of detected X-rays.

For these symmetrically shaped particles, it can be expected that total internal reflection plays an important role in the light outcoupling behavior,[44] especially when the particles are measured in vacuum or air, leading to a significant difference in refractive index at the
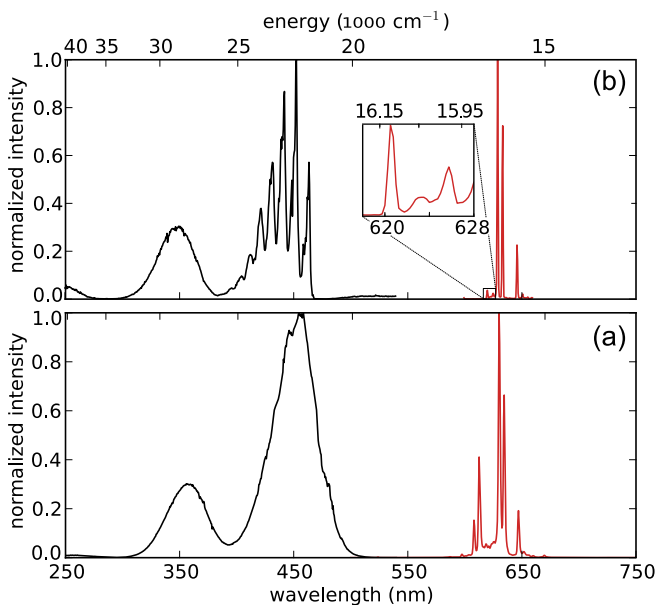

Figure 4. Photoluminescence excitation (upon monitoring emission at 630 nm) and emission (upon monitoring excitation at 455 nm) spectra of K_2SiF_6:Mn^{4+} measured at room temperature (a) and at 10 K (b).

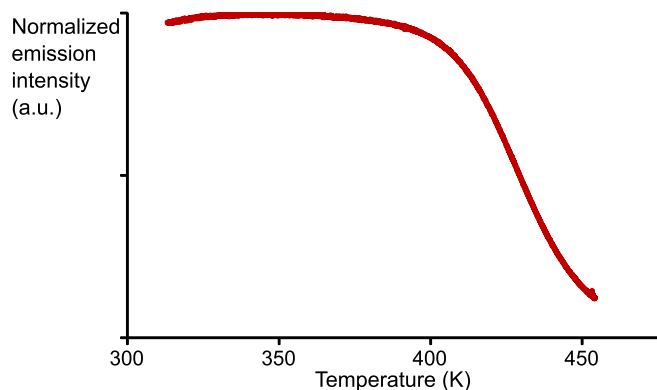**Figure 6.** Integrated emission intensity of K_2SiF_6:Mn^{4+} as a function of temperature.

Figure 8. Decay times (a–c) (boxes) and fraction of decay component (d) (bars, the full line is a guide to the eye) as a function of temperature of K_2SiF_6:Mn^{4+}. With increasing temperature a second, faster decay component (c) emerges. The effective decay time (b) (open boxes) is calculated as a weighted average of the two components (a) and (c).

faces of the crystals. The longer optical-path length will lower the final quantum efficiency as defects other than Mn^{4+}, which can be unintentionally present, might reabsorb the light and non-radiatively dissipate the energy. When K_2SiF_6 (refractive index of 1.34[18]) is embedded in epoxy or silicone binder material, the outcoupling from the phosphor particles will be improved.

Thermal properties.— Both the luminescent emission intensity and the luminescent lifetime were measured as a function of temperature. From the thermal-quenching measurements up to 450 K (Figure 6) the characteristic temperature $T_{1/2}$, for which the emission intensity is halved compared to the intensity at low temperature, is determined at 430 K. The emission intensity remains stable until 400 K, which is within the 400–450 K operating temperature of LED chips.[1] At 450 K, the emission intensity is lowered to 16% of the initial emission intensity. To increase the performance of the phosphor in high-power LEDs with elevated operating temperatures, a remote-phosphor approach can be used. By separating the phosphor layer from the LED chip, the operating temperature of the phosphor can be lowered due to the lower excitation flux. The thermal design should be such that the Stokes losses from the conversion process, which amount to 30% of the incident blue photon flux, are adequately removed from the remote phosphor plate.[45]

Heat treatment of the phosphor powder at 473 K in air left the luminescent properties intact, while heat treatment at 673 K caused a color change of the powder from light-yellow to brown and almost entirely destroyed the luminescence, with a remaining quantum efficiency of less than 1%. In SEM, some particles are still intact, but on other particles, structural changes from cubic crystals to amorphous shapes are detected. This is in agreement with the decomposition starting at 638 K as reported in literature.[17]
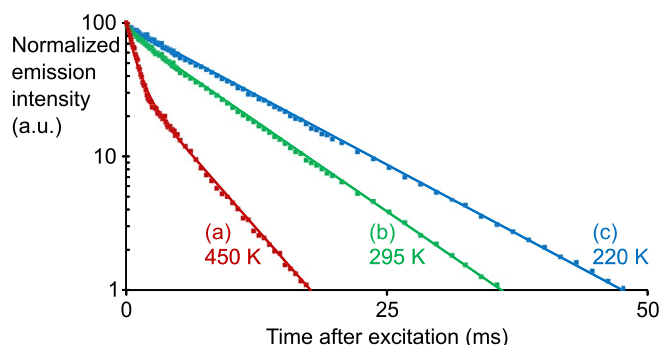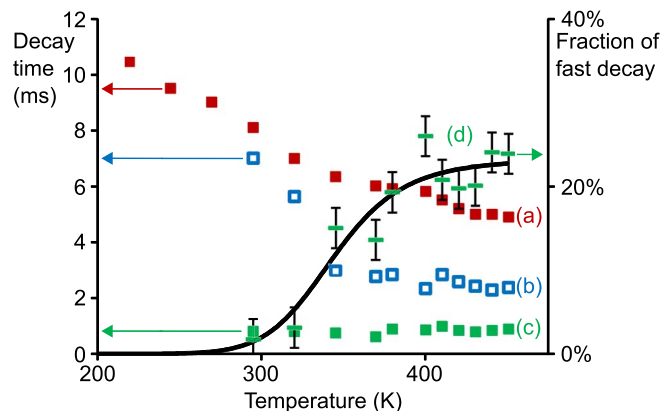

Figure 7. Decay profile measurements (dots) and fit (lines) of the luminescence intensity of K_2SiF_6:Mn^{4+} at 450 K (a), 295 K (b) and 220 K (c).

The luminescent-lifetime measurements in Figure 7 show a mono-exponential decay at 220 K with a decay time $\tau = 10.5$ ms. With increasing temperature (in the 295–450 K range), a bi-exponential decay is required since a second, faster decay component emerges. The time constant of the slow component (Figure 8a), decreases with increasing temperature, reaching $\tau = 8.1$ ms at room temperature and $\tau = 4.9$ ms at 450 K. This behavior is consistent with the drop in the overall decay time from 15 to 7 ms in the 20–300 K temperature range that was reported earlier.[30] Our results show that the drop in decay time continues further with increasing temperature, although thermal quenching only starts above 400 K.

The second, faster component (Figure 8c), has a decay time between 0.63 and 1.0 ms in the 295–450 K range. The fraction of the total emission assigned to the fast component increases from 2–3% in the 295–320 K temperature range to 15% at 345 K and 24% at 450 K (Figure 8d). An effective decay time (Figure 8b) is calculated as a weighted average of the two decay components.

The largest fraction of the emission, 76% at 450 K, takes place following the slower, spin-forbidden $^2E_g \rightarrow {}^4A_{2g}$ transition and no extra peaks are observed in the emission spectrum with increasing temperature.

From the particular shape of the decay curves, it is plausible to assume that a certain minority of the Mn^{4+} centers show different emission dynamics, provided that sufficient thermal energy is available. This energy allows the defect center to be thermally excited to an electronic eigenstate, characterized by a slightly higher total energy and a higher probability for radiative decay. In the case of perfectly-octahedral MnF_6^{2-} defect clusters, the degeneracy of the emitting ^2E_g level is maintained, even with the inclusion of spin–orbit coupling. In that case, the emitting level transforms according to the four-dimensional irreducible representation G (irrep) of the double group O_h^*. This is visualized in the modified Tanabe–Sugano diagram, displayed in Figure 9a. Therefore, the question is what the origin is of such a faster-decaying, higher-lying multiplet. In the following, it is examined through crystal field theory whether this can be the result of a small deformation of the octahedral complex, for example by nearby lattice defects or other Mn^{4+} ions.

Geometry of Mn^{4+} defects.— Two straightforward ways exist to lower the octahedral symmetry, either tetragonally by prolonging or shortening the body diagonal along a fourfold rotation axis or trigonally by altering the length of the body diagonal along a threefold rotation axis. Consequently, one ends up with respective point symmetries D_{4h} and D_{3d}. In Figures 9b and 9c, the effect of the deformation on the multiplets is given as a function of the Ballhausen $10Ds$ and $10D\sigma$ parameters, quantifying the deformations.[46] In both cases, it is
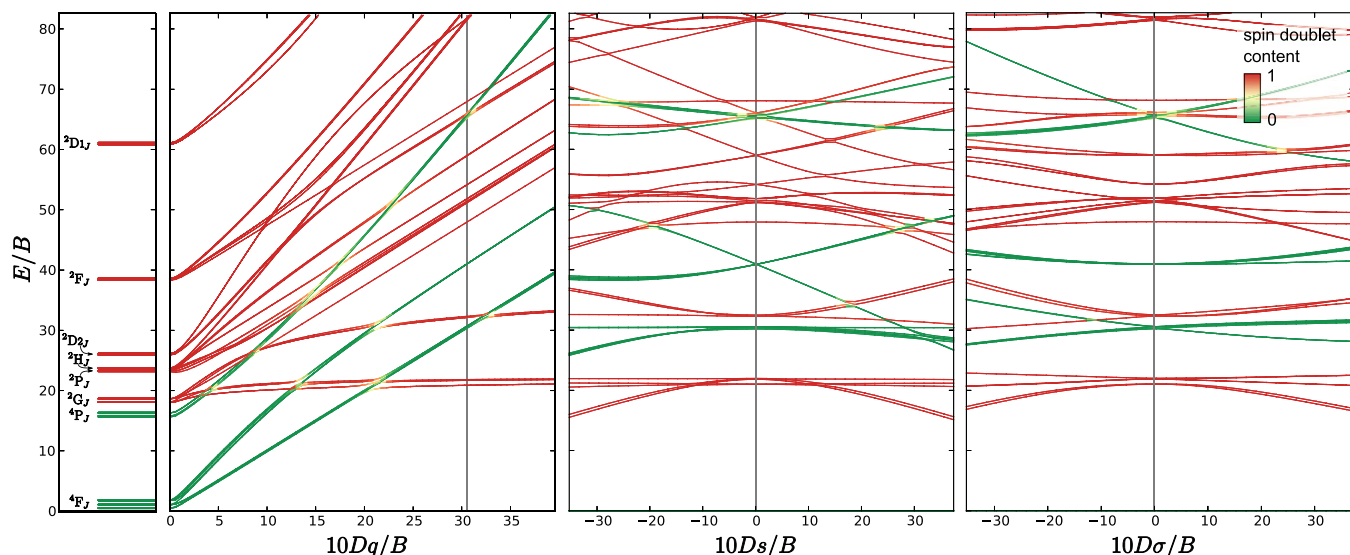
Figure 9. Tanabe–Sugano diagram of a d^3 configuration, originating from exact diagonalization of the effective Hamiltonian (Eq. 1) in octahedral symmetry and with the inclusion of spin–orbit coupling ($\zeta_{3d} = 47$ meV) (a). The effect of tetrahedral deformation of the octahedral Mn^{4+} defect ($O_h \rightarrow D_{4h}$) on the multiplet energies for a constant $10Dq = 30.2B$ and $Dt = 0$ (b). The effect of trigonal deformation of the octahedral Mn^{4+} defect ($O_h \rightarrow D_{3d}$) on the multiplet energies for a constant $10Dq = 30.2B$ and $D\tau = 0$ (c). The color of the lines represent the amount of spin quartet ($S = 3/2$) or doublet ($S = 1/2$) character of the eigenstate.

assumed that the cubic ratios of the crystal field parameters in octahedral symmetry are maintained during the deformation. The exact definition of the Ballhausen parameters and their relation with the conventional Wybourne parameters B_{kq} is provided in the Appendix.

In the case of a tetragonal deformation, the emitting ^2E_g multiplet splits into two singlets, transforming as the $^2A_{1g}$ and $^2B_{1g}$ irreps of D_{4h}, corresponding with the Kramers doublets $E_{1/2g}$ and $E_{5/2g}$. The ground-state multiplet $^4A_{2g}$ of O_h corresponds with the $^4B_{1g}$ irrep of D_{4h}. Due to the spin–orbit interaction, this level is split in two Kramers doublets, $E_{1/2g}$ and $E_{5/2g}$. If the selection rules for electric dipole transitions in D_{4h} symmetry are considered, every transition is forbidden due to the presence of an inversion center and Laporte's rule. If this parity selection rule is relaxed, or with other words, after a further descent of symmetry toward C_{4v}, one finds that the $B_1 \rightarrow B_1$ transition is electric-dipole allowed in this reduced symmetry, that is the direct product $B_1 \otimes A_1 \otimes B_1$ transforms according to the totally symmetric representation A_1 in C_{4v} symmetry. In this case, the z component of the electric dipole moment has symmetry label A_1. The $A_1 \rightarrow B_1$ transition remains symmetry forbidden at the electric dipole level as $A_1 \otimes A_1 \otimes B_1$, for polarization along the z axis, and $A_1 \otimes E \otimes B_1$, for polarizations perpendicular to the z axis, do not contain A_1 in their reduction. If the B_1 multiplet has a slightly higher energy than the A_1 multiplet, the particular decay behavior can be explained. This corresponds with negative Ds values. If the crystal field is parameterized in terms of a point-charge model, negative Ds and Dt values signify a shortening of the body diagonal of the coordination polyhedron. Tetragonal deformation can be expected in the K_2SiF_6 crystal from a nearby fluorine vacancy or interstitial atom. Interstitials might occupy the octahedral voids in the crystal structure (Wyckoff site 4b) and are indeed expected to compress the coordination polyhedron in the direction of the fourfold rotation axis.

In the case of a trigonal deformation, the ^2E_g multiplet does not split due to symmetry breaking, but rather transforms as the irrep ^2E_g of D_{3d}. However, unlike the octahedral case, this multiplet splits in two Kramers doublets, $E_{1/2g}$ and $E_{3/2g}$ due to spin–orbit interaction. In the case of positive $10D\sigma$ values, the higher-lying Kramers doublet features a slightly higher $S = 3/2$ content than the lower-lying one, ensuring a faster decay due to a relaxation of the spin selection rule. However, the weak spin–orbit interaction for 3d ions mixes spin multiplicity only in a limited way. Typically 0.2–0.5% of quartet character is present in the relevant eigenstates. This is also clear from Figure 9. Only where energy levels are sufficiently close to interact,

substantial spin mixing is visible. For this reason, it is more likely that the observed decay behavior originates from tetragonal deformation rather than from trigonal deformation. Electron paramagnetic resonance (EPR) offers an experimental way to distinct one case from the other. Trigonal deformation is induced when two Mn^{4+} ions are incorporated on neighboring Si^{4+} sites in the crystal or from an adjacent potassium vacancy.

From symmetry arguments, it is most likely that the observed decay dynamics originate from a tetragonal compression of the coordination polyhedron. For this reason, the crystal-field Hamiltonian for D_{4h} symmetry was fit to the experimental low-temperature photoluminescence spectrum. Racah, spin–orbit and Trees parameters were kept fixed at literature values that were obtained for similar Mn^{4+} systems.[14,47,48] The crystal field $10Dq$ and $10Ds$ values were varied in order to reproduce the experimental transition energies as good as possible. The location of the ZPLs of the $^4A_{2g} \rightarrow {}^4T_{2g}$ and $^4A_{2g} \rightarrow {}^4T_{1g}$ transitions were assigned to the low energy side of the respective excitation bands. The crystal field splitting between the $^2B_{1g}$ and $^2A_{1g}$ multiplets was estimated in the order of $kT \approx 250$ cm^{-1} from the activation temperature of the fast decay component. The fixed and optimized parameters are summarized in Table I, the optimized energies are tabulated in Table II. The root-mean-square deviation of the fit is 270 cm^{-1}, which is reasonable given the limited number of experimentally available energies.

Saturation behavior.— Previous reports claim no light-induced degradation in K_2SiF_6:Mn^{4+},[49] but at high laser power, both saturation and degradation of the phosphor occur. In Figure 10, the measured emission intensity is plotted as a function of excitation power. The

Table I. Parameters used in the crystal field calculation.

Parameter	Value (cm^{-1})	Reference
B	770	14
C	3470	14
ζ_{3d}	380	47
α	91	47,48
$10Dq$	21791	
$10Ds$	−1118	
$10Dt$	0	

Table II. Calculated multiplet energies, obtained from a crystal field calculation, compared to the experimental parameters, obtained from low-temperature PL spectroscopy.

O_h	D_{4h}	Calculation (cm^{-1})	Experiment (cm^{-1})
$^4A_{2g}$	$^4B_{1g}$	0.00	0.00
		0.16	
^2E_g	$^2A_{1g}$	16166	16117
	$^2B_{1g}$	16406	≈ 16360
$^2T_{1g}$	^2E_g	16685	
		16837	
	$^2A_{2g}$	17456	
$^4T_{2g}$	^4E_g	21166	21553
		21167	
		21186	
		21234	
	$^4B_{2g}$	21827	
		21888	
$^2T_{2g}$	$^2B_{2g}$	25118	
	^2E_g	25882	
		26012	
$^4T_{1g}$	^4E_g	27671	27300
		27758	
		27828	
		27919	
	$^4A_{2g}$	33052	
		33082	

expected linear response of the emission intensity to increasing excitation power, when no saturation occurs, is shown as a dotted line (Figure 10b). At about 40 W/cm² the sublinear response becomes appreciable, which puts an upper limit on the incident excitation flux. The emission intensity (full line in Figure 9) can be fitted according to:

$$I_{em} = IQE \cdot I_{exc} \cdot A \cdot [N_0 / (I_{exc} A \cdot \tau(T) - I_{exc} A P_{ESA} \cdot \tau(T) + N_0)]$$

[2]

In this equation, IQE is the internal quantum efficiency of the phosphor, I_{exc} is the excitation intensity (increasing with increasing laser power), A is the absorption probability of incident light on the phos-
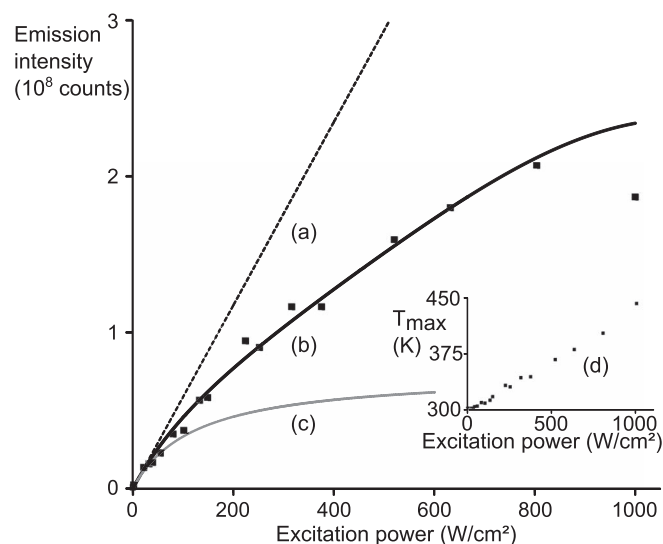
phor (decreasing with increasing laser power), N_0 is the number of Mn ions exposed to the laser spot, $\tau(T)$ is the effective decay time, which is a function of the sample temperature (Figure 8b) and P_{ESA} is the probability of excited-state absorption. The absorption probability A and the probability for excited-state absorption P_{ESA}, were varied to calculate the emission intensity as a function of excitation power. The parameters were optimized using the least-squares minimization.

The rise in temperature (see inset of Figure 10) of the phosphor powder with increasing laser intensities was estimated using an IR camera. At low laser power, the sample temperature was 300 K, close to the ambient temperature. The last data point (at 440 K) of the emission intensity was excluded from the fit, as thermal quenching takes place and some irreversible degradation sets in.

The temperature dependency of the effective decay time, as was shown in Figure 8, was specifically included in the simulation, because an obvious temperature increase is caused by the high laser flux, due to non-radiative de-excitations and Stokes losses following the absorption of blue photons. The effect of this is visible when the black line (Figure 10b) is compared to the gray line (Figure 10c), which is the simulated emission intensity with a fixed decay time, as found at room temperature. Here, saturation sets in earlier, because less Mn ions are available for excitation due to the longer lifetime of the emitting state. With increasing excitation power, the absorption probability decreases, because a large fraction of the Mn ions is in the excited state, making less ions available from excitation from the ground state (ground-state depletion). In this situation, the excited ions will eventually give light emission, but no further blue-photon absorption is possible.

Another saturation mechanism is possible, when an ion in the excited state absorbs another blue photon, followed by a non-radiative transition to the ground state. This excited-state absorption results in no emission from two absorbed blue photons. The probability for excited-state absorption was varied in the simulation, but its contribution turned out to be negligible, so the saturation behavior of K_2SiF_6:Mn^{4+} can be adequately explained without including excited-state absorption. However, pump–probe absorption spectroscopy should be performed to assess the extent of excited state absorption in this phosphor.

Saturation cannot be fully relieved by the decreasing decay time at higher temperatures, but the decrease in absorption probability is less severe compared to the case of a fixed decay time due to a decrease in decay time down to 2.3 ms at 800 W/cm². The sublinear response to the emission intensity starts to appear at an excitation power of 40 W/cm², where 11% of the available Mn ions are in the excited state.

After saturating the sample with a blue laser up to 1500 W/cm², the sample was damaged on the location of the laser spot. A structural change is visible in the SEM picture in Figure 11a, showing large, 100 µm diameter spheres instead of cubic phosphor crystals as in pristine material. EDX and CL mappings were sampled on the damaged area (right, dotted line) and outside the laser spot (bottom left, full line). The CL mapping in Figure 11b shows almost no emission in the damaged area. The EDX spectrum in Figure 11c shows a change in composition, with a drop in the F Kα signal in the degraded sample (dotted line) and an increase of Si Kα and O Kα.

These results show that the studied phosphor might be useful for low-power white LEDs, but not for high-power applications, where the long decay time of the phosphor leads to saturation effects. For the latter application, a remote-phosphor approach can be used: by increasing the distance between the exciting LED and the phosphor, both the thermal load and the optical load on the phosphor are strongly reduced.

Application in white LEDs.— The narrow red emission of K_2SiF_6:Mn^{4+} complements the yellow and blue emission of phosphor-converted white LEDs as is simulated in Figure 12. Due to the large offset between the excitation and emission bands in the spectrum of K_2SiF_6:Mn^{4+}, there is no reabsorption of YAG:Ce emission by the red phosphor. Therefore, the phosphor-converted white LED can be

Figure 10. Saturation of K_2SiF_6:Mn^{4+} at high laser power (445 nm): measurements (dots), simulation of saturation with temperature-dependent decay time (b) (black line), simulation of saturation with fixed decay time (c) (gray) and simulation of linear response (a) (dotted line); and sample temperature at the laser spot (d) (inset).
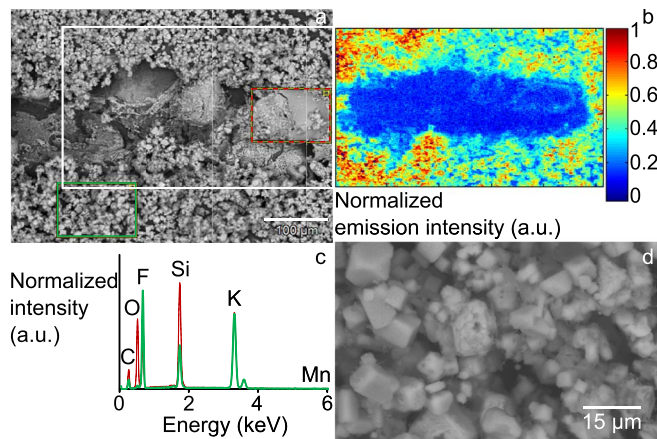
Figure 11. SEM image of the laser-induced degradation of the phosphor (a), CL mapping for the area indicated by the large white rectangle (b), EDX spectrum (c) for the pristine (red dashed rectangle in (a)) and the degraded part (green rectangle in the bottom left of (a)), SEM picture of phosphor particles treated for one hour at 673 K in air (d).
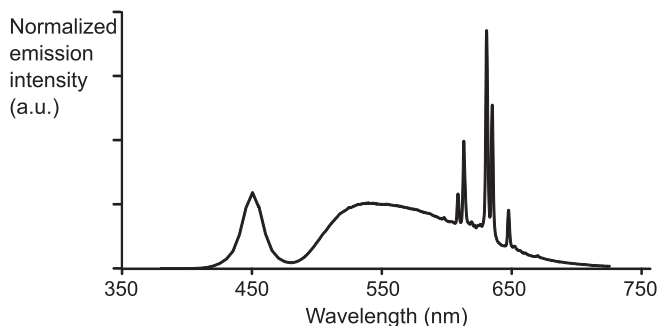

Figure 12. Simulated spectrum of a white phosphor-converted LED using YAG:Ce and K_2SiF_6:Mn^{4+} with red phosphor content $x = 0.27$, resulting in a CCT of 3466 K, a CRI of 90 and a LER of 337 lm/W.

simulated by weighted addition of the emission spectra of a blue LED, YAG:Ce and K_2SiF_6:Mn^{4+}. In Figures 13 and 14, x is the K_2SiF_6:Mn^{4+} content, while 1-x is the YAG:Ce content in the total phosphor amount. The emission spectra are normalized on the number of emitted photons, implying an internal quantum efficiency of 100%. For each x, the D_{uv} value (the shortest distance of the LEDs color point to the blackbody locus in the CIELuv color space) is minimized by varying the ratio between the blue emission from the LED and the yellow and red emission from the phosphor blend to find an optimal white LED. By minimizing D_{uv} the correlated color temperature is automatically fixed. The total amount of phosphor used increases with higher content of K_2SiF_6:Mn^{4+}, because more phosphor emission is needed to reach the blackbody locus at low color temperatures.

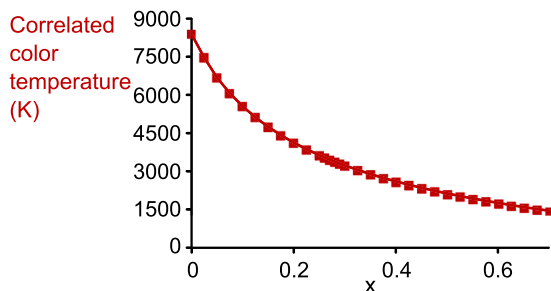**Figure 13.** Range of correlated color temperature (CCT) for a white phosphor-converted LED with YAG:Ce and K_2SiF_6:Mn^{4+} phosphors.
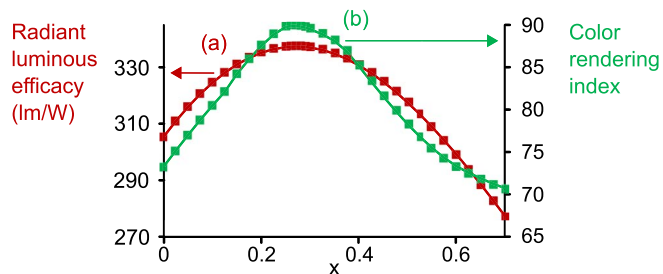

Figure 14. Radiant luminous efficacy (LER) (a) and color rendering index (CRI) (b) for a white phosphor-converted LED with YAG:Ce and K_2SiF_6:Mn^{4+} phosphors.

When increasing the amount of K_2SiF_6:Mn^{4+} in the phosphor mixture, the correlated color temperature (CCT) in Figure 13 drops from 8376 K for pure YAG:Ce to 2700 K for 61.7% YAG:Ce. Both the radiant luminous efficacy (LER) and the color rendering index (CRI) in Figure 14 reach a maximum value for $x = 0.27$. For $x > 0.6$, the values of both CRI and LER drop below the values of a YAG:Ce white LED. The addition of K_2SiF_6:Mn^{4+} to YAG:Ce in a phosphor-converted white LED can improve the properties, but only within a specific range of phosphor combinations. The optimal combination of 63% YAG:Ce and 27% K_2SiF_6:Mn^{4+} in Figure 12, results in a CCT of 3466 K, a CRI of 90 and a LER of 337 lm/W. These results are consistent with phosphor combinations reported in literature, where the combination of K_2SiF_6:Mn^{4+} and YAG:Ce with a blue LED chip provided warm-white LEDs with a CRI of 89.9 and wall–plug efficiency of 116 lm/W[17] or a CRI of 90.9 and wall–plug efficiency of 81.56 lm/W.[43]

Conclusions

K_2SiF_6:Mn^{4+} shows red line emission around 630 nm with a main excitation band around 455 nm, ideal for blue LED excitation. An internal quantum efficiency of 42% is found, which can be further improved. A dopant concentration of 8% was used in the precursor solution, but only a limited incorporation of Mn in the phosphor crystals occurs during the synthesis, leading to an actual dopant concentration of 1.5% of the Si ions.

At low temperatures (220 K), a mono-exponential decay is found, while a bi-exponential decay emerges with increasing temperature in the 295–450 K range. The decay time continues to decrease with increasing temperature up to 450 K, although thermal quenching only starts above 400 K.

The faster decay component which emerges at elevated temperatures is attributed to a certain fraction of the Mn^{4+} dopants that are incorporated in close vicinity of another point defect. The different possibilities were examined through crystal field calculations. In the case of tetragonal deformation, the symmetry selection rule is relaxed, while in the case of trigonal deformation, the spin selection rule is relaxed. Given the limited strength of the spin–orbit interaction in the 3d shell of Mn^{4+}, the observed decay behavior is more likely to originate from tetragonal distortion.

High incident fluxes cause both saturation of the emission and degradation of K_2SiF_6:Mn^{4+}. Above 40 W/cm^2, there is a sublinear response of the emission intensity to the excitation power, caused by ground-state depletion. Saturation cannot be fully relieved by the decreasing decay time at higher temperatures. Furthermore, incident fluxes up to 1500 W/cm^2 lead to a structural change in the phosphor particles, a change in composition and almost no CL emission.

At the microscopic level, combined SEM-EDX-CL mappings show a preferential location of the light output on certain edges of the cubic particles. Since total internal reflection plays an important role in the light outcoupling behavior of symmetrically shaped particles, it is within expectations that higher emission intensities are found at

distortions of the cubic shape. Besides cubic particles, different types of truncated particle shapes are found.

An optimal warm-white LED is simulated using 27% K$_2$SiF$_6$:Mn^{4+} and 63% YAG:Ce, with a CCT of 3466 K, a CRI of 90 and a LER of 337 lm/W. A remote-phosphor approach is proposed to increase the performance of K$_2$SiF$_6$:Mn^{4+} in conditions where the operating temperature or the incident fluxes exceed 400 K or 40 W/cm^2, respectively. By increasing the distance between the exciting LED and the phosphor, both thermal quenching and saturation due to the long, ms range, decay time of K$_2$SiF$_6$:Mn^{4+} can be relieved.

Appendix: Parameterization of the Crystal Field

Different parameterizations of the crystal field are available in literature. In the present case, the tetragonal and trigonal deformation of an octahedral crystal field is investigated. A special parameterization was developed by Ballhausen to describe these kinds of deformation.[46,50,51] The relationship between the Ballhausen and more conventional Wybourne parameterization is described in this appendix.

Octahedral crystal field, O$_h$.— Two possible parameterizations of the crystal field are possible within the Wybourne scheme, with respect to a fourfold rotation axis or with respect to a threefold rotation axis. If the z-axis of the reference frame is along a fourfold axis, the crystal field Hamiltonian for a d^N configuration reads:

$$\mathcal{H}_{cf}^{(4)} = \sum_{i=1}^{N} B_{40}^{(4)} \left[C_{40}(i) + \sqrt{5/14} \left(C_{44}(i) + C_{4\,-4}(i) \right) \right]$$

As one can see, two crystal field parameters, B_{40} and B_{44}, are nonzero, although their ratio is fixed at the *cubic ratio* $\sqrt{5/14}$ and only one independent parameter remains.[36] The superscript (4) denotes the reference system and is added to avoid confusion.

It is customary to introduce the parameter 10Dq, often denoted as Δ, in this geometry. It signifies the energy difference between the e_g and t_{2g} orbitals in a d^1 configuration in an octahedral field:

$$10Dq = \frac{10}{21} B_{40}^{(4)}$$

In the context of a general d^N configuration, the meaning of 10Dq is less obvious due to term splitting.

Alternatively, the crystal field Hamiltonian can be written with respect to a reference system where the z-axis is put along the threefold rotation axis:

$$\mathcal{H}_{cf}^{(3)} = \sum_{i=1}^{N} B_{40}^{(3)} \left[C_{40}(i) + \sqrt{10/7} \left(C_{43}(i) - C_{4\,-3}(i) \right) \right]$$

In this case one is left with the B_{40} and B_{43} parameters which are mutually connected by the cubic ratio $\sqrt{10/7}$. When the same physical system is described, one has the following relationship:

$$B_{40}^{(3)} = -\frac{2}{3} B_{40}^{(4)}.$$

Tetrahedral symmetry, D$_{4h}$.— When the symmetry is lowered to D$_{4h}$, the crystal field Hamiltonian is:

$$\mathcal{H}_{cf} = \sum_{i=1}^{N} \left[B_{20}C_{20}(i) + B_{40}C_{40}(i) + B_{44}(i) \left(C_{44}(i) + C_{4\,-4}(i) \right) \right].$$

Three independent parameters are thus required. An alternative parameterization is used by Ballhausen:

$$B_{20} = -7D_s$$

$$B_{40} = 21 \left(Dq - Dt \right)$$

$$B_{44} = 21\sqrt{5/14}Dq$$

Ds is related to the extra Wybourne parameter that emerges from the descent of the symmetry. Dt describes the deviation from the cubic ratio. Only when $Dt = 0$, the relationship between B_{40}, B_{44} and Dq is the same as in the case of octahedral symmetry.

Trigonal symmetry, D$_{3d}$.— For D$_{3d}$ symmetry, the crystal field Hamiltonian becomes:

$$\mathcal{H}_{cf} = \sum_{i=1}^{N} \left[B_{20}C_{20}(i) + B_{40}C_{40}(i) + B_{43}(i) \left(C_{43}(i) - C_{4\,-3}(i) \right) \right].$$

Again, three independent parameters are required. A similar alternative parameterization is again available:

$$B_{20} = -7D\sigma;$$

$$B_{40} = -14Dq - 21D\tau;$$

$$B_{43} = -2\sqrt{70}Dq.$$

When $D\tau = 0$, the relationship between B_{40}, B_{43} and Dq is the same as in the case of octahedral symmetry when referred to the threefold axis.

References

1. P. F. Smet, A. B. Parmentier, and D. Poelman, *J. Electrochem. Soc.*, **158**, R37 (2011).
2. P. F. Smet, I. Moreels, Z. Hens, and D. Poelman, *Materials*, **3**, 2834 (2010).
3. N. Avci, J. Musschoot, P. F. Smet, K. Korthout, A. Avci, C. Detavernier, and D. Poelman, *J. Electrochem. Soc.*, **156**, J333 (2009).
4. Y.-S. Kim, S.-W. Choi, J.-H. Park, E. Bok, B.-K. Kim, and S.-H. Hong, *ECS J. Solid State Sci. Technol.*, **2**, R3021 (2012).
5. P. Pust, V. Weiler, C. Hecht, A. Tücks, A. S. Wochnik, A.-K. Henß, D. Wiechert, C. Scheu, P. J. Schmidt, and W. Schnick, *Nat. Mater.*, **13**, 891 (2014).
6. Y. Q. Li, J. E. J. van Steen, J. W. H. van Krevel, G. Botty, A. C. A. Delsing, F. J. DiSalvo, G. de With, and H. T. Hintzen, *J. Alloys Compd.*, **417**, 273 (2006).
7. R. Cao, M. Peng, E. Song, and J. Qiu, *ECS J. Solid State Sci. Technol.*, **1**, R123 (2012).
8. M. G. Brik and A. M. Srivastava, *J. Lumin.*, **133**, 69 (2013).
9. M. G. Brik, S. J. Camardello, and A. M. Srivastava, *ECS J. Solid State Sci. Technol.*, **4**, R39 (2014).
10. M. A. Noginov and G. B. Loutts, *J. Opt. Soc. Am. B*, **16**, 3 (1999).
11. Z. Bryknar, V. Trepakov, Z. Potůček, and L. Jastrabík, *J. Lumin.*, **87**, 605 (2000).
12. M. G. Brik, A. M. Srivastava, and N. M. Avram, *Opt. Mater.*, **33**, 1671 (2011).
13. S. Adachi and T. Takahashi, *J. Appl. Phys.*, **104**, 023512 (2008).
14. T. Takahashi and S. Adachi, *J. Electrochem. Soc.*, **155**, E183 (2008).
15. S. Adachi and T. Takahashi, *Electrochem. Solid-State Lett.*, **12**, J20 (2009).
16. T. Takahashi and S. Adachi, *Electrochem. Solid-State Lett.*, **12**, J69 (2009).
17. L. Lv, X. Jiang, S. Huang, X. Chen, and Y. Pan, *J. Mater. Chem. C*, **2**, 3879 (2014).
18. M. G. Brik and A. M. Srivastava, *J. Electrochem. Soc.*, **159**, J212 (2012).
19. M. Novita and K. Ogasawara, *Jpn. J. Appl. Phys.*, **51**, 022604 (2012).
20. T. Arai and S. Adachi, *Jpn. J. Appl. Phys.*, **50**, 092401 (2011).
21. J. H. Oh, H. Kang, Y. J. Eo, H. K. Park, and Y. R. Do, *J. Mater. Chem. C*, **3**, 607 (2015).
22. A. A. Setlur, E. V. Radkov, C. S. Henderson, J.-H. Her, A. M. Srivastava, N. Karkada, M. S. Kishore, N. P. Kumar, D. Aesram, A. R. Deshpande, B. Kolodin, S. G. Ljudmil, and U. Happek, *Chem. Mater.*, **22**, 4076 (2010).
23. J. E. Murphy, A. A. Setlur, F. Garcia, R. J. Lyons, A. I. Chowdhury, N. Karkada, and P. K. Nammalwar, US Pat. 8,906,724 (2014).
24. R. J. Lyons, A. A. Setlur, A. R. Deshpande, and L. S. Grigorov, US Pat. 8,252,613 (2012).
25. S. H. Jo, S. H. Yoon, W. P. Lee, and H. J. Kim, US Pat. 20140043810 (2014).
26. V. Weiler, W. Schnick, P. J. Schmidt, and M. A. Seibald, US Pat. 20140320788 (2014).
27. M. Kim, W. B. Park, C. H. Kim, K.-S. Sohn, and B. K. Bang, *J. Mater. Chem. C*, **4**, 1166 (2015).
28. A. A. Setlur, J. J. Shiang, and U. Happek, *Appl. Phys. Lett.*, **92**, 081104 (2008).
29. S. Adachi, H. Abe, R. Kasa, and T. Arai, *J. Electrochem. Soc.*, **159**, J34 (2012).
30. R. Kasa and S. Adachi, *J. Electrochem. Soc.*, **159**, J89 (2012).
31. H. Nguyen, C. C. Lin, M. Fang, and R. Liu, *J. Mater. Chem. C*, **2**, 10268 (2014).
32. Y. Ohno, in *SPIE Fourth International Conference on Solid State Lightning.*, **5530**, 88 (2004).
33. Y. Ohno, *Opt. Eng.*, **44**, 111302 (2005).
34. W. Davis and Y. Ohno, in *Proceedings of SPIE*. I. T. Ferguson, J. C. Carrano, T. Taguchi, and I. E. Ashdown, Editors, **5941**, 59411G (2005).
35. N. M. Avram and M. G. Brik, *Optical Properties of 3d-Ions in Crystals: Spectroscopy and Crystal Field Analysis*, Springer, Berlin, (2013).
36. C. Görller-Walrand and K. Binnemans, in *Handbook on the Physics and Chemistry of Rare Earths*. K. A. Gschneider and L. Eyring, Editors, **23**, 155, North-Holland, Amsterdam, Netherlands (1996).
37. B. R. Judd, *Operator Techniques in Atomic Spectroscopy*, Princeton University Press, Princeton, NJ, (2014).
38. G. Racah, *Phys. Rev.*, **85**, 381 (1952).
39. R. E. Trees, *Phys. Rev.*, **85**, 382 (1952).

40. R. E. Trees and C. K. Jørgensen, *Phys. Rev.*, **123**, 1278 (1961).
41. Python Software Foundation, Python Language Reference, version 2.7. http://www.python.org.
42. R. D. Shannon, *Acta Crystallogr. Sect. A*, **32**, 751 (1976).
43. C. Liao, R. Cao, Z. Ma, Y. Li, G. Dong, K. N. Sharafudeen, and J. Qiu, *J. Am. Ceram. Soc.*, **96**, 3552 (2013).
44. K. Korthout, P. F. Smet, and D. Poelman, *Appl. Phys. Lett.*, **94**, 051104 (2009).
45. M. Meneghini, M. Dal Lago, N. Trivellin, G. Meneghesso, and E. Zanoni, *IEEE Trans. Device Mater. Reliab.*, **13**, 316 (2013).
46. C. J. Ballhausen, *Introduction to Ligand Field Theory*, McGraw-Hill, New York, (1970).
47. C. A. Morrison, *Crystal Fields for Transition-Metal Ions in Laser Host Materials*, Springer, Berlin, (1992).
48. W. Li, *At. Data Nucl. Data Tables*, **2**, 45 (1970).
49. T. Oyama and S. Adachi, *J. Appl. Phys.*, **116**, 133515 (2014).
50. M. Gerloch and R. C. Slade, *Ligand Field Parameters*, Cambridge University Press, Cambridge, U.K., (2009).
51. Z. Y. Yang and Q. Wei, *Phys. B Condens. Matter*, **370**, 137 (2005).